Geophysical Research Letters

RESEARCH LETTER
10.1029/2021GL093912

Directionality of the Martian Surface Radiation and Derivation of the Upward Albedo Radiation

Jingnan Guo[1,2,3], Salman Khaksarighiri[3], Robert F. Wimmer-Schweingruber[3], Donald M. Hassler[4], Bent Ehresmann[4], Cary Zeitlin[5], Sven Löffler[3], Daniel Matthiä[6], Thomas Berger[6], Günther Reitz[6], and Fred Calef[7]

[1]School of Earth and Space Sciences, University of Science and Technology of China, Hefei, PR China, [2]CAS Center for Excellence in Comparative Planetology, USTC, Hefei, PR China, [3]Institute of Experimental and Applied Physics, Christian-Albrechts-University, Kiel, Germany, [4]Planetary Science Division, Southwest Research Institute, Boulder, CO, USA, [5]Leidos Corporation, Houston, TX, USA, [6]German Aerospace Center (DLR), Institute of Aerospace Medicine, Cologne, Germany, [7]Jet Propulsion Laboratory, California Institute of Technology, Pasadina, CA, USA

Abstract Since 2012 August, the Radiation Assessment Detector (RAD) on the Curiosity rover has been characterizing the Martian surface radiation field which is essential in preparation for future crewed Mars missions. RAD observed radiation dose is influenced by variable topographical features as the rover traverses through the terrain. In particular, while Curiosity was parked near a butte in the Murray Buttes area, we find a decrease of the dose rate by $(5 \pm 1)\%$ as 19% of the sky was obstructed, versus 10% in an average reference period. Combining a zenith-angle-dependent radiation model and the rover panoramic visibility map leads to a predicted reduction of the downward dose by ~12% due to the obstruction, larger than the observed decrease. With the hypothesis that this difference is attributable to albedo radiation coming from the butte, we estimate the (flat-terrain) albedo radiation to be about 19% of the total surface dose.

Plain Language Summary Interplanetary space is filled with energetic particles that can affect the health of astronauts, for example, by causing late-arising cancer and possibly hereditary diseases. Mars lacks a global magnetic field and its atmosphere is very thin compared to Earth's. Thus its surface is exposed to such space radiation which presents risks to future humans on Mars. Mitigation strategies could include using natural geological structures on Mars, for example, cave skylights and lava tubes and even simple buttes, for protection. The Radiation Assessment Detector (RAD) on the Curiosity rover has observed a decrease of the radiation absorbed dose rate by $(5 \pm 1)\%$ while Curiosity was parked near a butte. This provides the first direct illustration that Mars's surface features may serve as potential radiation shelters for future missions. However, when exploiting such shielding possibilities, the secondary radiation generated in the terrain of Mars that is, emitted backwards must also be considered. Combining the RAD observation with a radiation transport model, we derive such "reflected" radiation dose on a flat terrain to be about 19% of the total surface dose.

Key Points:

- The Martian surface radiation is influenced by topographical features
- The surface downward radiation dose of particles traversing through the atmosphere depends on the zenith angle
- The surface upward radiation dose is about 19% of the total dose

Correspondence to:

J. Guo and S. Khaksarighiri,
jnguo@ustc.edu.cn;
khaksari@physik.uni-kiel.de

Citation:

Guo, J., Khaksarighiri, S., Wimmer-Schweingruber, R. F., Hassler, D. M., Ehresmann, B., Zeitlin, C., et al. (2021). Directionality of the Martian surface radiation and derivation of the upward albedo radiation. *Geophysical Research Letters*, *48*, e2021GL093912. https://doi.org/10.1029/2021GL093912

Received 19 APR 2021
Accepted 9 JUL 2021

1. Introduction

Health risks induced by exposure to space radiation have been classified as one of the potential "show stoppers" for future human missions to Mars (e.g., Cucinotta et al., 2017; Walsh et al., 2019). To evaluate such radiation risks, the Radiation Assessment Detector (RAD, Hassler et al., 2012; Zeitlin et al., 2016) was designed to measure energetic particle radiation on the Martian surface (Hassler et al., 2014) as part of the Mars Science Laboratory (MSL, Grotzinger et al., 2012) mission, which landed the Curiosity rover in Gale crater in August 2012.

Space radiation near Mars is contributed by the continuous background Galactic Cosmic Ray (GCR) particles and, occasionally, Solar Energetic Particles (SEPs) resulting from solar eruptions. Mars lacks a global intrinsic magnetosphere but has a thin atmosphere. The primary space radiation can directly propagate through the atmosphere with no interactions or lose part of its energy and generate secondaries via ionization, fragmentation, spallation, etc. Secondary particles can also be generated in the terrain and escape the surface to be detected as upward-directed "albedo" particles. The Martian radiation environment can be studied via particle transport modeling through the Martian atmosphere and surface (De Angelis et al., 2006;

Ehresmann et al., 2011; Gronoff et al., 2015; Keating et al., 2005; Kim et al., 2014; Saganti et al., 2004; etc). The successful operation of RAD on Mars also made it possible to benchmark these models against in-situ measurements (e.g., Matthiä et al., 2016, 2017; Guo et al., 2019).

The Radiation Assessment Detector consists of three silicon detectors (A, B, and C, each having a thickness of 300 μm), a thallium-doped cesium iodide scintillator (D with a thickness of 28 mm), and a plastic scintillator (Bicron BC432 m, E with a thickness of 18 mm and mass of 34.9 gram). In particular, the absorbed dose rate, defined as the energy deposited by radiation per unit mass (Gray = J/kg) and time, is measured concurrently in two active dosimeters, that is, detectors B and E. The latter has much better statistics due to a large geometric factor. It has a composition similar to that of human tissue and is more sensitive to neutrons. Additionally, low-energy albedo particles traveling upward from the surface are likely to deposit energy in E but may stop in the detector stack (or scatter out of the stack) before reaching B. Therefore, we use the absorbed dose in the plastic detector "E" in this study.

The Martian topographic structures may serve for radiation shielding for future human missions on Mars. They can be particularly helpful to provide shielding during highly intense SEP events and can also serve to achieve a steady reduction of exposure to the long-term GCR-induced radiation (Dartnell et al., 2007; Kim et al., 1998; Röstel et al., 2020). Locations with higher iron and/or hydrogen content can also be beneficial especially via moderating the neutron contribution to radiation as suggested by models (Da Pieve et al., 2021; Keating & Gonçalves, 2012; Masarik & Reedy, 1996; Röstel et al., 2020). In order to evaluate potential regolith shielding strategies, it is essential to correctly model particle interactions with the Martian surface material. The assessment of surface albedo radiation is therefore important as it is a direct result of radiation interaction in the Martian terrain.

Particles coming into RAD from all directions can contribute to the recorded dose. However, the directionality of the incoming particle is not registered in the dose-rate data, and it is not possible to directly assess the observed albedo radiation. In this study, we estimate the contribution of albedo dose using a Martian atmosphere radiation model anchored to the RAD measurements. The model provides the angular dependence of the downward-directed dose as it would be measured by RAD if it had this capability (Section 2). The measurements are taken before and during a period when the rover was parked close to a butte with a portion of the downward-directed dose blocked by the butte structure (Section 3). We then derive the first observation-based assessment of the Martian surface albedo dose (Section 4) and find that it is about 19% of the total surface dose on a flat terrain without obstructions.

2. The Zenith Angle Dependence of the Dose

Wimmer-Schweingruber et al. (2015) have studied the zenith angle (θ, the angle from the surface normal) dependence of the particle fluxes reaching RAD and found that the radiation field is nearly, but not entirely isotropic for $\theta \leq \sim 15°$. In order to better understand the directionality of the dose on the surface of Mars over a wide range of zenith angles ($0° \leq \theta \leq 90°$), we construct a Monte Carlo model of GCRs propagating through the Martian atmosphere, which allows to derive the dose dependence on θ.

The input primary GCRs are obtained using the Badhwar-O'Neill (BON) 2014 prescription of solar modulation, which solves the Fokker–Planck equations to transport the local interstellar GCR spectrum to 1 AU (O'Neill et al., 2015). The intensity of GCRs is modulated by solar activity and heliospheric magnetic field, which evolve with the 22-year solar Hale cycle (Potgieter, 2013). The strength of the modulation is quantified by the so-called "modulation potential Φ" in the BON model, which is normally determined monthly. We assume the monthly averaged GCR spectra to be the same at Mars since the radial gradient of GCR flux in the heliosphere is only about 1%–2% between 1 AU and 1.5 AU (within 10 AU) according to multi-spacecraft observations (Honig et al., 2019; Roussos et al., 2020).

We calculate the interaction of primary GCRs with the Martian atmosphere represented by a spherical shell of CO_2 gas using the GEANT4 particle transport code (Agostinelli et al., 2003). The vertical atmospheric mass ($\theta = 0°$) is set as 21 g/cm^2, which approximately corresponds to an average surface pressure of ~800 Pa as measured by MSL's Rover Environmental Monitoring Station (REMS, Gómez-Elvira et al., 2012). The thickness of the atmosphere increases with θ to account for a realistic 3D atmospheric structure. Only

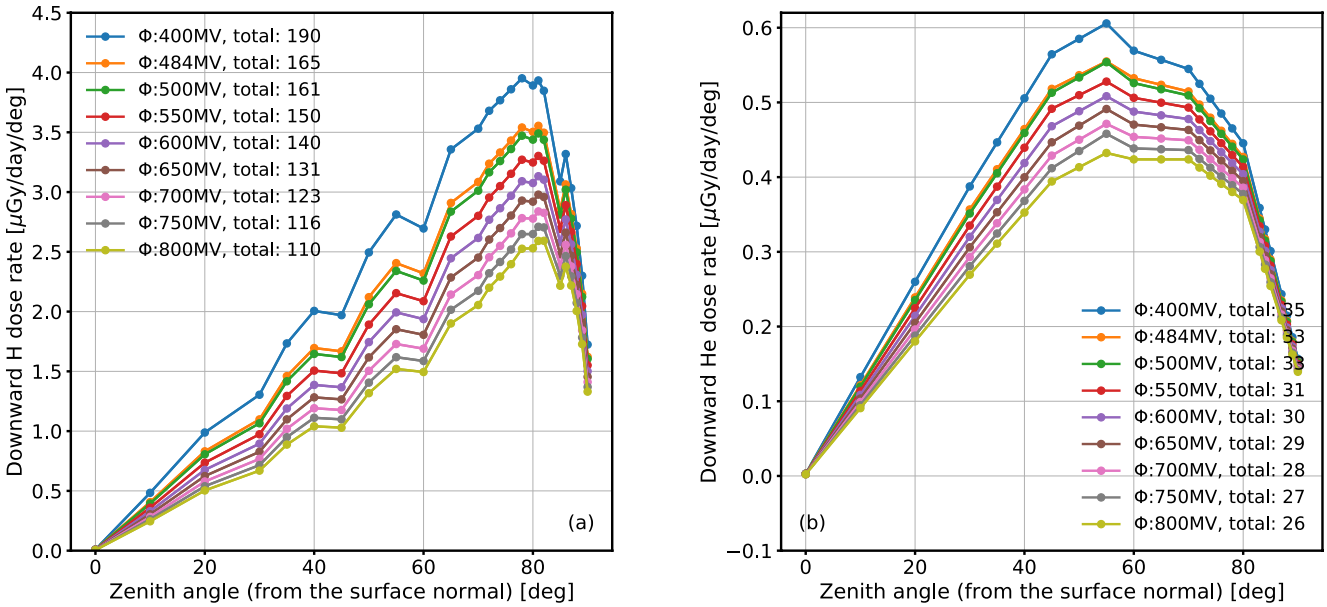

Figure 1. Simulation results for the dependence of dose rate on zenith angle, θ, of (a) incoming primary GCR protons and (b) helium ions. Different primary GCR spectra are considered under different solar modulation potentials Φ, as inputs to the BON model, as explained in Section 2. The total dose rates [μGy/day] integrated over θ are also given in each case.

protons and helium ions are modeled as they make up about 99% of the GCR atomic nuclei (Simpson, 1983). Heavier ion contributions to the surface dose will be additionally considered in Section 4. All primary and secondary particles tracked in the model that reach RAD can also interact with the RAD detectors and contribute to absorbed dose. As the simulated particle direction is known, we can track the dose, as would be measured by the RAD E detector, contributed by particles arriving from specific zenith angles. The physics list QGSP_BERT has been used in the current model setup. Although the model selection in GEANT4 may affect the calculated secondary particle spectra, the surface absorbed dose agrees within ~5% for different physics lists (Matthiä et al., 2016).

The modeled zenith-angle dependence of the dose rate in RAD E detector is shown in Figure 1 for primary protons and helium ions under different solar modulation potential Φ. As shown, the surface dose rate depends on solar modulation, with a smaller Φ (weaker modulation) resulting in a larger dose rate for each θ. The dose rate summed over θ from 0 to 90° represents the total downward-directed dose rate on the surface for each Φ value. The dose induced by primary protons is 4.2–5.4 times (depending on Φ) larger than that induced by primary helium ions.

The modeled results show that radiation on Mars is dependent on θ. For example, protons coming in at θ~80° make the greatest contribution to the surface dose per angular bin. For helium ions, this angle is at around 55°. Two factors drive this result: (1) transport through larger depths of atmosphere at larger zenith angle θ and (2) simple geometry, since the solid angle subtended at large zenith angles is greater for each degree of θ than at smaller angles. The transport effects can be qualitatively understood by considering that the atmospheric column depth increases from about 21 g/cm^2 at θ = 0° to more than 300 g/cm^2 at angles above 85°. These longer paths slow primaries substantially which become more ionizing or more easily stopped; meanwhile, the probability of the initial ion undergoing a nuclear interaction and fragmenting into lighter ions is higher with a thicker path.

One can scale the dose rate in Figure 1 by the geometric factor of each θ to remove the area effect (so that the y-axis has units of μGy/day/cm^2/sr). The scaled proton functions (not plotted here) have a more gradual increase before the major peak at $\theta \sim 80°$ (with a column depth of 110 g/cm^2) followed by a secondary peak at $\theta \sim 86°$. As described above, the primary peak arises from the combination of primary protons slowing down and the efficient generation of secondary particles. The secondary peak is due to the fact that particles arriving from near-horizontal directions have longer paths in the hexagonal prism-shaped RAD E detector

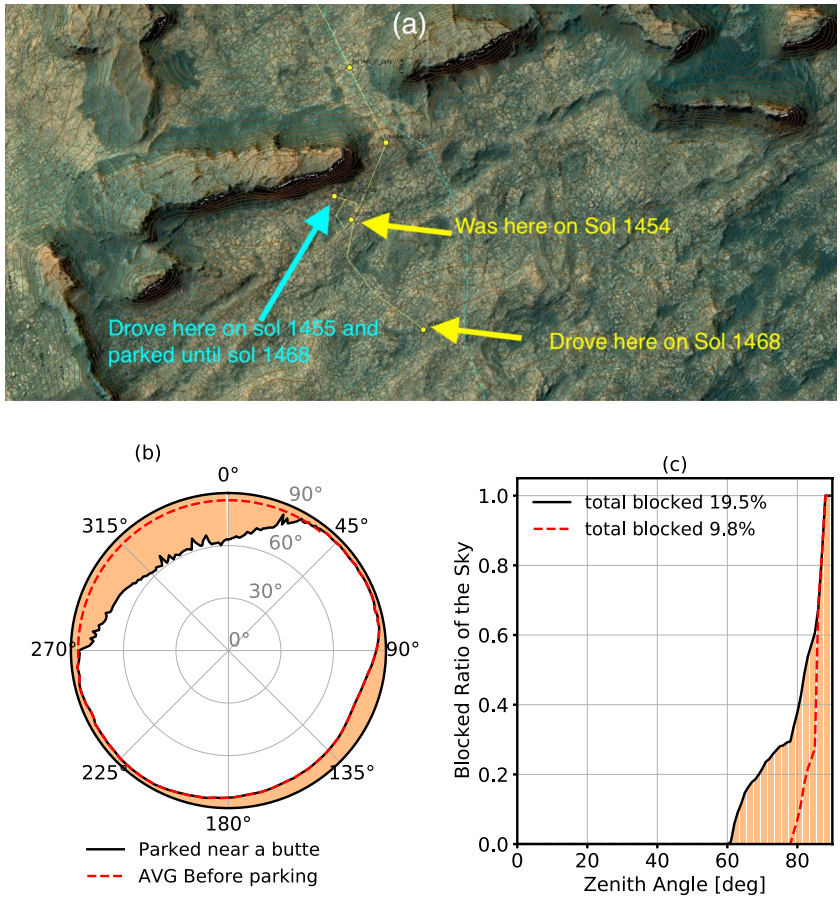

Figure 2. (a) The rover traverse map through the Murray Buttes area (North is up.). Each drive is marked as the path between the yellow dots where the rover stopped. The locations before, after, and during the 13-sol parking are marked. The base image is adapted from here https://mars.nasa.gov/resources/38045/curiosity-rovers-location-for-sol-1468/. (b) The panoramic sky visibility of RAD as a function of the 360° of azimuth angle (0° for North). The zenith angle of obstructed view during the 13-sol parking is shown in orange shaded area. Surface particles can directly reach RAD from the non-shaded area. The red dashed curve shows the sky view averaged for periods before the parking as described in Section 4. (c): The ratio of blocked sky as a function of the zenith angle for the two periods. The integrated value is shown for each period.

compared to those arriving from smaller zenith angles. On the other hand, the scaled helium dose (not plotted here) decreases monotonically with increased θ (so as column depth) since helium ions have smaller mean free paths and are more likely to fragment in a thicker atmosphere.

Figure 1a also shows some bumpy features from ~30° to 60°, which are due to a combination of uncertainties in the transport calculations and statistical variations. (Using smoothed functions without such features, we performed the analysis throughout this work and found the exact same result with a precision of 1 μGy/day.)

3. The Reduction of Radiation Due to Topographical Shielding at Murray Buttes

The Curiosity rover has been exploring Gale crater while gradually climbing up Mount Sharp, which forms the central peak within the crater. In September 2016, Curiosity traversed through a geological formation called "Murray Buttes" (MB), which contains mesas and buttes consisting of eroded sandstone (Byrne, 2020). The relevant rover traverse path is shown in Figure 2a. [A Martian day (sol) lasts 24 h and 39 min. Mission progress is measured in sols since landing.] On Sol 1455 (2016-09-08), the rover drove close to a butte as pointed out by the cyan arrow and was subsequently parked there for nearly 13 sols to perform

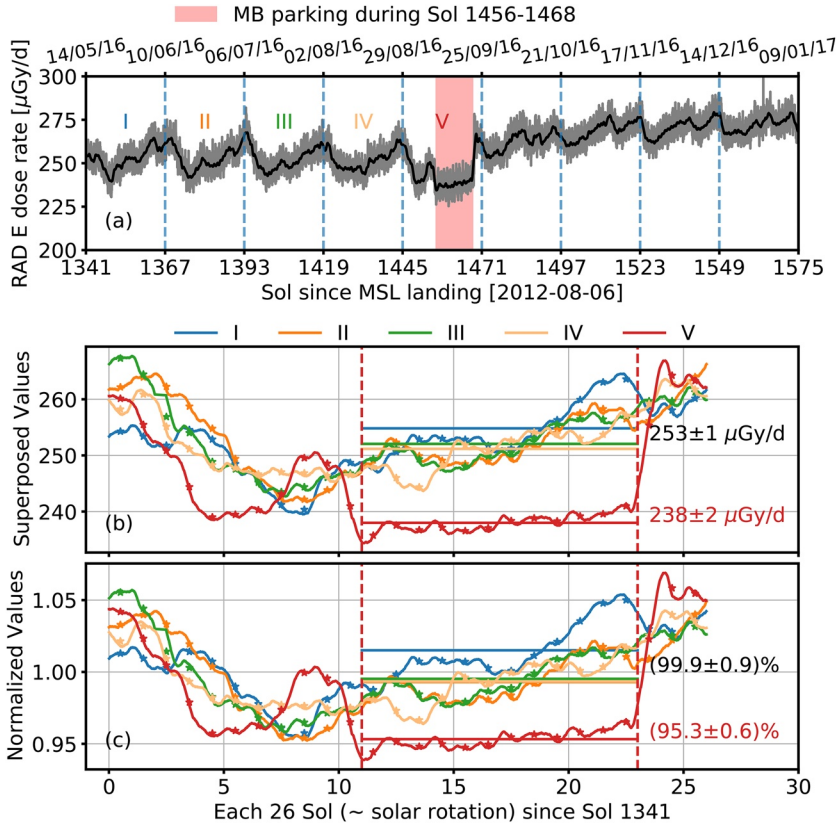

Figure 3. (a): The RAD E dose rate measurement from May 2016 until January 2017. Original data are in gray, and smoothed daily values are in black. Each solar rotation cycle of about 26 sols is separated by dashed lines. (b): Superposed daily dose rates for the five rotations which are marked from I to V in (a). The time of each rotation ranges from sol 1 until 26. The period, when Curiosity was parked, is shaded in red in (a) and marked between dashed vertical lines in (b). The average dose rate during the parking and the average dose rate for cycles I to IV between the dashed lines are marked. (c): The same as (b), but with the normalized dose rate. See Section 3 for more details.

drilling and contact science operations and drove away from the butte on Sol 1468. Figures 2b and 2c shows the obstructed fraction of the sky during the course and will be discussed in Section 4.

GCR flux in the heliosphere can be modulated by the recurrent heliospheric structures, called corotating interaction regions (CIRs), which often appear during the declining phase of a solar cycle (e.g.., Crooker et al., 1999; Richardson, 2004). CIRs are formed when high speed solar wind streams arising from coronal holes (CHs) run into preceding slow solar wind in the interplanetary space. As CHs may exist stably for several solar rotations, the consequent GCR modulation occurs periodically. Geyer et al. (2021) have studied the evolution of CIRs at Mars and Earth using *in situ* solar wind and magnetic field data as well as remote-sensing solar images of the CHs. They found that there are multiple CHs and corresponding CIRs reappearing for at least five solar rotations from the end of May until the end of September 2016.

As shown in Figure 3a, the RAD measured dose rate repeats very similar evolutionary patterns throughout this period including four solar rotational cycles (marked as I–IV) followed by a cycle "V," which contains the MB parking (shaded in red). The regularity of GCR variation in the subsequent cycles started to deteriorate as the CIRs became unstable due to the evolution of the solar CHs, which often experience growing and decaying phases (Heinemann et al., 2018). Therefore, if no topographical influence were present, dose rate throughout cycles I–V should repeat similar temporal evaluations. However, as shown, there is a sudden drop and a quick recovery of the RAD dose rate at the start and end of the parking period. The fundamental reason is that a portion of the sky is blocked by the butte where downward particles are stopped from reaching RAD directly. Nevertheless, because the dose rate varies with time, we need to derive this reduction excluding the background variation due to the above-discussed heliospheric influences.

We then superpose and analyze the RAD dose rate measured throughout solar rotational cycles I–V. The daily dose rate of each cycle is re-plotted with a time span of 26 sols in Figure 3b. The dose rate during ~13 sols of MB parking as marked between dashed vertical lines is substantially lower than that recorded in the same window of the previous four cycles. The average dose rate of the MB parking period is 238 ± 2 μGy/d and is 253 ± 1 μGy/d for cycles I–IV in this window with a difference of 15 ± 2 μGy/d due to the butte's obstruction.

Considering that there is a slight variation of the long-term GCR flux throughout the five cycles, for each cycle, we also normalized the data by the mean value of the data outside the dashed-line-delimited window and repeat the superpose analysis (see Figure 3c). The normalized data are averaged as (99.9 ± 0.9)% during this window for cycles I–IV and are (95.3 ± 0.6)% during the parking, resulting in a drop ratio of 5% ± 1% between the two.

4. The Derivation of Regolith-Generated Albedo Radiation

The panoramic angle of obstructed view (AOV, angle from the horizon) of the sky seen by RAD during the MB parking of the rover is shown in Figure 2b. The AOV ranges from ~3° from the horizon ($\theta = 87°$) upto about 30° ($\theta = 60°$). The butte obstruction of the sky is mainly found at azimuth angle $\phi < 40°$ and $\phi > 265°$. Before the parking, the rover was driving through the MB area and did not have a full view of the sky either. Therefore, for this period, we approximate the AOV at $\phi < 40°$ and $\phi > 265°$ using the median value of AOV at other azimuth angles, which is 4.13°. Such derived AOV, averaged for months before the parking, is shown as the red-dashed curve. Considering that each zenith angle corresponds to a 1°-wide ring area of the 2π full-sky sphere, we calculate the ratio of the obstructed area (ROA) as shown in Figure 2c, for the two periods. At $\theta > 85°$, the ROA is above 80% in both periods. The total blocked ratio of the sky integrated over θ is about 0.19 for the period of MB parking and about 0.10 averaged before the parking.

Previously, the model of zenith-angle dependence of the dose (Section 2 and Figure 1) gives the dose functions $d_{\mathrm{H}}(\theta)$ and $d_{\mathrm{He}}(\theta)$ for proton and helium ions, respectively. Combining the dose-θ functions and the RAD sky view, we can calculate the expected dose rate contributed by particles arriving from the sky direction as:

$$D_{\mathrm{GCR_H}} = \sum_{\theta=0°}^{90°} (1 - \mathrm{ROA}(\theta)) \cdot d_{\mathrm{H}}(\theta) \tag{1}$$

$$D_{\mathrm{GCR_{He}}} = \sum_{\theta=0°}^{90°} (1 - \mathrm{ROA}(\theta)) \cdot d_{\mathrm{He}}(\theta). \tag{2}$$

The term $1 - \mathrm{ROA}(\theta)$ is the unblocked ratio of the sky as also plotted in Figure 4a under three different topographical arrangements (as explained later). Additionally, primary GCRs heavier than protons and helium ions contribute nearly 10% to the total absorbed dose on the surface of Mars as suggested by results of simulations using the atmospheric condition at Gale crater (Röstel et al., 2020). Therefore, we approximate the total dose rate contributed by all GCRs arriving from the sky direction as:

$$D_{sky} = 1.10 \cdot (D_{\mathrm{GCR_H}} + D_{\mathrm{GCR_{He}}}) \tag{3}$$

Now, we consider three topographical scenarios and the corresponding dose rate derived from the combination of the dose-zenith model (Figure 1) and ROA observation (Figure 2b) as following.

(a) For a completely flat terrain without any surface obstruction, $1 - \mathrm{ROA}(\theta)$ is constantly unity as $\mathrm{ROA}(\theta)$ is simply zero, shown as "a full sky-view" in Figure 4a. The solar modulation potential Φ during 2016 September is about 484 MV used for the BON model (the orange curves in Figure 1). Following Equation 1, we derive $D^a_{\mathrm{GCR_H}} = 165$ μGy/d induced by primary protons and their secondaries and $D^a_{\mathrm{GCR_{He}}} = 33$ μGy/d from primary helium ions and their secondaries, which result in $D^a_{\mathrm{sky}} = 218$ μGy/d (Equation 3). The corresponding calculations are also shown as azure curves in Figure 4b.

(b) Before the parking, folding the sky-view function b) in Figure 4a with the modeled $d_{\mathrm{H}}(\theta)$ and $d_{\mathrm{He}}(\theta)$ under the average modulation Φ of 500 MV from May–August 2016 (the green curves in Figure 1), we

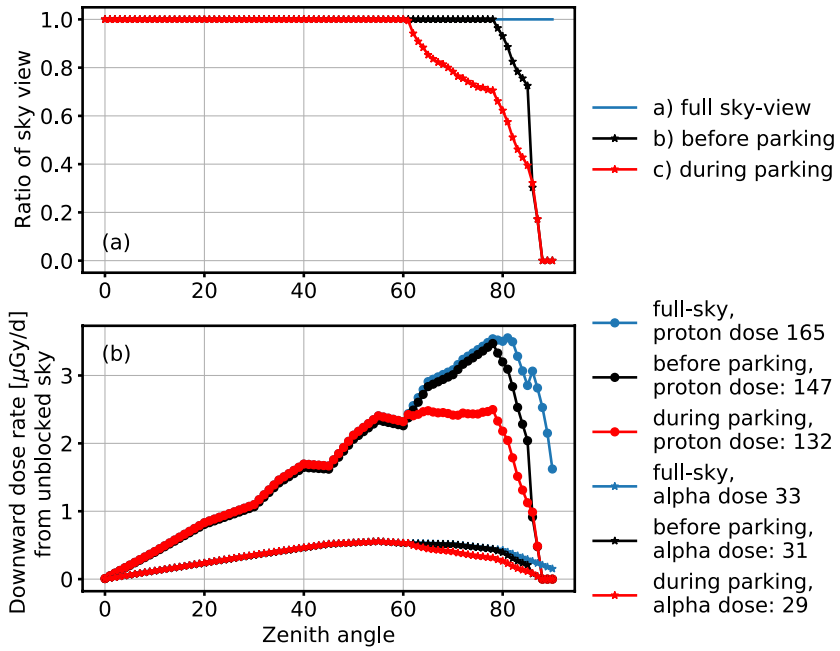

Figure 4. (a) The unblocked ratio of the sky as a function of the zenith angle θ for three geospatial scenarios: (a) full sky view, (b) before the MB parking, and (c) during the MB parking. (b): The dose rate resulting from particles arriving from the sky as a function of θ for primary GCR protons (filled circles) and helium ions (stars) under the three different scenarios. In each case, the dose rate integrated over θ is marked in the legend.

obtain $D^b_{\mathrm{GCR_H}} = 147$ μGy/d and $D^b_{\mathrm{GCR_{He}}} = 31$ μGy/d, which lead to $D^b_{\mathrm{sky}} = 196$ μGy/d, shown as black curves in Figure 4b. Note that Φ of 484 MV (for September 2016) would result in 201 μGy/d, which is about 92% of the full-sky dose D^a_{sky} under the same Φ.

(c) During the parking, with the sky-view function c) in Figure 4a, we obtain $D^c_{\mathrm{GCR_H}} = 132$ μGy/d and $D^c_{\mathrm{GCR_{He}}} = 29$ μGy/d, which result in $D^c_{\mathrm{sky}} = 177$ μGy/d, shown as red lines in Figure 4b. This is about 81% of the full sky-view dose D^a_{sky} and 90% of the dose rate D^b_{sky} before the parking or 88% of the dose rate in scenario (b) if the exact same solar modulation is present. In other words, radiation from the atmosphere reaching RAD decreased by about 12% during the parking caused by sky obstruction of the nearby butte.

Such estimated decrease is much larger than the observed 4%–6% (Section 3) because the butte blocked the radiation from the sky but meanwhile contributing to the albedo radiation. The interaction of particles with the Martian regolith happens mostly within the uppermost 2 m of the subsurface as modeled by Röstel et al. (2020, Figure 2). The model also suggests that the albedo radiation detected as dose changes little as the soil composition varies (Figure 4 of the article). We then assume that albedo radiation generated by the butte is similar to that from the ground regolith, and the total albedo dose only depends on the effective geometric area of the regolith source.

Defining the dose rate contributed by a completely flat terrain to be D_{albedo}, that is, when the sky or terrain contributes an exact half of the full 4π solid angle, we formulate the total dose rate on a terrain with obstructions as below:

$$\left(1 + \sum_{\theta=0^\circ}^{90^\circ} \mathrm{ROA}(\theta)\right) D_{\mathrm{albedo}} + D_{\mathrm{sky}} = D_{\mathrm{total}}, \tag{4}$$

where $\sum_{\theta=0^\circ}^{90^\circ} \mathrm{ROA}(\theta)$ is the total blocked ratio of the sky that contributes alternatively to the albedo radiation and is about 0.19 during the MB parking and 0.10 averaged before the parking (Figure 2). D_{sky} is the remaining dose of particles propagating from the atmosphere and has been derived for above different scenarios. Scenario (a) is however unrealistic for the Curiosity rover inside Gale crater which almost always

provides some viewing obstructions. Applying scenario (b) with $D_{sky} = 196$ μGy/d and the estimated dose rate $D_{total} \approx 253$ μGy/d before the parking (Figure 3), we obtain $D_{albedo} \approx 52$ μGy/d. Similarly, for scenario (c) during the parking, that is, $D_{sky} = D^{c}_{sky} = 177$ μGy/d and $D_{total} \approx 238$ μGy/d, we obtain $D_{albedo} \approx 51$ μGy/d. It is remarkable how well the two estimates agree.

This gives the first estimation of the Martian surface albedo radiation dose based on synergistic assessments of modeled results and *in situ* observations. The ratio of such estimated albedo radiation, 51–52 μGy/d, to the downward radiation on a flat terrain, D^{a}_{sky}, is about 23% and is about 19% to the total surface dose. The albedo contribution is slightly higher when there are surface obstructions as expected, for example, about 21% with 10% blockage of the sky. It is in good agreement with the 18%–20% upward dose ratio obtained from GEANT4 particle transport models (Guo et al., 2018; Matthiä & Berger, 2017) but larger than that modeled by Kim et al. (2014), which is only about 10%. More topographic information collected at other locations in combination with RAD measurements can further verify and improve our assessment and may also be able to provide a "radiation map" along the path of the Curiosity rover. Moreover, different solar activities, surface elevations or Martian seasons may also affect the albedo contribution and surface radiation. A low elevation and consequently a thicker atmosphere can also enhance the shielding effect as observed by RAD (Guo et al., 2017; Rafkin et al., 2014).

5. Discussion and Conclusion

The Martian surface radiation is influenced by surface topographical features. While Curiosity was parked near a butte in the Murray Butte area, we found the butte structure, blocking out about 19% of the sky (vs. 10% in the preceding period), induced a decrease of the background GCR dose by (5 ± 1)%. Although this reduction is not significant enough to fully protect future astronauts from cosmic radiation on Mars, it illustrates that existing natural structures such as buttes, cave skylights (Cushing et al., 2007), or lava tubes (Léveillé & Datta, 2010) may serve as a potential radiation shelter for future habitats on Mars, benefiting from the grander strategy of *in situ* resource utilization (Starr & Muscatello, 2020). For instance, the modeled radiation environment on and under the surface of Mars suggests that ~1 m of shielding depth may limit the annual absorbed dose in water within 20 mGy (Röstel et al., 2020).

Due to the varying atmospheric column depth for particles arriving from different zenith angles θ, the surface downward radiation dose of particles is θ dependent. We have modeled this process and provided the dose-θ functions for different solar modulation conditions and particle types. This model is then used in combination with the RAD panoramic visibility map to derive the obstructed and remaining radiation coming from the sky direction. The ratio of the radiation from the sky during the parking compared to that before the parking is estimated to be about 88% assuming the same solar modulation condition. This reduction of 12% is significantly higher than the observed (5 ± 1)% of dose decrease. This is because the obstructing butte contributes to additional albedo radiation.

Accounting for the expected dose reduction due to the sky blockage and observed dose changes, we derive the flat-terrain (i.e., zero obstruction) albedo dose to be about 19% of total surface dose based on two independent scenarios. This result is consistent with previous modeled results (Guo et al., 2018; Matthiä et al., 2017). Appel et al. (2018) have studied the charged protons detected in RAD's vertical telescope cone (with a half angle of 18°) and found a 10% ratio of the upward to downward flux of 100–200 MeV protons. This ratio is different from what we obtain here mainly for two reasons: (1) dose is contributed by all particles over a wide energy range and cannot be represented solely by protons in this energy range and (2) downward particles within the semi-vertical cone used in Appel et al. (2018) traverse through a much thinner atmosphere than those coming from more horizontal directions so that the downward flux/dose ratio in this cone is different from the averaged downward value.

In summary, the Martian surface radiation is influenced by local topographical features which change as the rover traverses through Gale crater. Detailed comparison of dose rates measured under different sky-obstruction conditions combined with zenith-angle dependence of the radiation allow us to estimate the contribution of the albedo radiation on Mars, which is an important assessment for better understanding the Martian radiation environment and developing radiation mitigation strategies.

Data Availability Statement

MSL/RAD data are archived in the NASA planetary data systems (https://pds.nasa.gov/ds-view/pds/viewDataset.jsp?dsid=MSL-M-RAD-3-RDR-V1.0). Data plotted in the figures are archived at Zonedo https://doi.org/10.5281/zenodo.4701689.

Acknowledgments
RAD is supported by NASA (HEOMD) under JPL subcontract 1273039 to SWRI, and in Germany by DLR (under German Space Agency grants 50QM0501, 50QM1201, and 50QM1701) to the CAU Kiel. J. G. is supported by the Strategic Priority Program of the Chinese Academy of Sciences (Grant No. XDB41000000), the National Natural Science Foundation of China (Grant No. 42074222) and the CNSA pre-research Project on Civil Aerospace Technologies (Grant No. D020104). Open access funding enabled and organized by Projekt DEAL.

References

Agostinelli, S., Allison, J., Amako, K., Apostolakis, J., Araujo, H., Arce, P., et al. (2003). GEANT4: A simulation toolkit. *Nuclear Instruments & Methods in Physics Research, Section A*, *506*(3), 250–303.

Appel, J. K., Köhler, J., Guo, J., Ehresmann, B., Zeitlin, C., Matthiä, D., et al. (2018). Detecting upward directed charged particle fluxes in the Mars Science Laboratory Radiation Assessment Detector. *Earth and Space Science*, *5*(1), 2–18. https://doi.org/10.1002/2016EA000240

Byrne, C. J. (2020). Murray and Stimson Formations, Murray Buttes, and the Dune Campaign. In *Travels with curiosity* (pp. 69–94). Springer. https://doi.org/10.1007/978-3-030-53805-7_7

Crooker, N. U., Gosling, J. T., Bothmer, V., Forsyth, R. J., Gazis, P. R., Hewish, A., et al. (1999). CIR morphology, turbulence, discontinuities, and energetic particles. *Space Science Reviews*, *89*, 179–220. https://doi.org/10.1023/A:1005253526438

Cucinotta, F. A., To, K., & Cacao, E. (2017). Predictions of space radiation fatality risk for exploration missions. *Life Sciences and Space Research*, *13*, 1–11. https://doi.org/10.1016/j.lssr.2017.01.005

Cushing, G. E., Titus, T. N., Wynne, J. J., & Christensen, P. R. (2007). THEMIS observes possible cave skylights on Mars. *Geophysical Research Letters*, *34*, 17201. https://doi.org/10.1029/2007GL030709

Da Pieve, F., Gronoff, G., Guo, J., Mertens, C., Neary, L., Gu, B., & Cleri, F. (2021). Radiation environment and doses on mars at oxia planum and Mawrth Vallis: Support for exploration at sites with high biosignature preservation potential. *Journal of Geophysical Research: Planets*, *126*(1), e2020JE006488. https://doi.org/10.1029/2020je006488

Dartnell, L., Desorgher, L., Ward, J., & Coates, A. (2007). Modeling the surface and subsurface martian radiation environment: Implications for astrobiology. *Geophysical Research Letters*, *34*, L02207. https://doi.org/10.1029/2006gl027494

De Angelis, G., Wilson, J. W., Clowdsley, M. S., Qualls, G. D., & Singleterry, R. C. (2006). Modeling of the Martian environment for radiation analysis. *Radiation Measurements*, *41*(9–10), 1097–1102. https://doi.org/10.1016/j.radmeas.2006.04.032

Ehresmann, B., Burmeister, S., Wimmer-Schweingruber, R. F., & Reitz, G. (2011). Influence of higher atmospheric pressure on the martian radiation environment: Implications for possible habitability in the Noachian epoch. *Journal of Geophysical Research: Space physics*, *116*(A15), 10106. https://doi.org/10.1029/2011ja016616

Geyer, P., Temmer, M., Guo, J., & Heinemann, S. G. (2021). Properties of stream interaction regions at Earth and Mars during the declining phase of sc 24. *Astronomy & Astrophysics*, *649*, A80. https://doi.org/10.1051/0004-6361/202040162

Gómez-Elvira, J., Armiens, C., Castañer, L., Domínguez, M., Genzer, M., Gómez, F., et al. (2012). REMS: The environmental sensor suite for the Mars Science Laboratory rover. *Space Science Reviews*, *170*(1–4), 583–640. https://doi.org/10.1007/s11214-012-9921-1

Gronoff, G., Norman, R. B., & Mertens, C. J. (2015). Computation of cosmic ray ionization and dose at Mars. I: A comparison of HZETRN and planetocosmics for proton and alpha particles. *Advances in Space Research*, *55*(7), 1799–1805. https://doi.org/10.1016/j.asr.2015.01.028

Grotzinger, J. P., Crisp, J., Vasavada, A. R., Anderson, R. C., Baker, C. J., Barry, R., et al. (2012). Mars Science Laboratory mission and science investigation. *Space Science Reviews*, *170*(1), 5–56. https://doi.org/10.1007/s11214-012-9892-2

Guo, J., Banjac, S., Röstel, L., Terasa, J. C., Herbst, K., Heber, B., & Wimmer-Schweingruber, R. F. (2019). Implementation and validation of the GEANT4/AtRIS code to model the radiation environment at Mars. *Journal of Space Weather and Space Climate*, *9*(A2), A7. https://doi.org/10.1051/swsc/2019004

Guo, J., Slaba, C., Tony, C., Zeitlin Wimmer-Schweingruber, R. F., Badavi, F. F., Böhm, E., et al. (2017). Dependence of the martian radiation environment on atmospheric depth: Modeling and measurement. *Journal of Geophysical Research: Planets*, *122*(2), 329–341. https://doi.org/10.1002/2016JE005206

Guo, J., Zeitlin, C., Wimmer-Schweingruber, R. F., McDole, T., Kühl, P., Appel, J. C., et al. (2018). A generalized approach to model the spectra and radiation dose rate of solar particle events on the surface of Mars. *The Astronomical Journal*, *155*(1), 49. https://doi.org/10.3847/1538-3881/aaa085

Hassler, D. M., Zeitlin, C., Wimmer-Schweingruber, R. F., Böttcher, S. I., Martin, C., Andrews, J., et al. (2012). The Radiation Assessment Detector (RAD) investigation. *Space Science Reviews*, *170*(1), 503–558. https://doi.org/10.1007/s11214-012-9913-1

Hassler, D. M., Zeitlin, C., Wimmer-Schweingruber, R. F., Ehresmann, B., Rafkin, S., Eigenbrode, J. L., et al. (2014). Mars's surface radiation environment measured with the Mars Science Laboratory's curiosity rover. *Science*, *343*(6169), 1244797.

Heinemann, S. G., Temmer, M., Hofmeister, S. J., Veronig, A. M., & Vennerstrøm, S. (2018). Three-phase Evolution of a Coronal Hole. I. 360° Remote Sensing and In Situ Observations. *The Astrophysical Journal*, *861*, 151. https://doi.org/10.3847/1538-4357/aac897

Honig, T., Witasse, O. G., Evans, H., Nieminen, P., Kuulkers, E., Taylor, M. G. G. T., et al. (2019). Multi-point galactic cosmic ray measurements between 1 and 4.5 AU over a full solar cycle. *Annales Geophysicae*, *37*(5), 903–918. https://doi.org/10.5194/angeo-37-903-2019

Keating, A., & Gonçalves, P. (2012). The impact of mars geological evolution in high energy ionizing radiation environment through time. *Planetary and Space Science*, *72*(1), 70–77. https://doi.org/10.1016/j.pss.2012.04.009

Keating, A., Mohammadzadeh, A., Nieminen, P., Maia, D., Coutinho, S., Evans, H., et al. (2005). A model for Mars radiation environment characterization. *IEEE Transactions on Nuclear Science*, *52*(6), 2287–2293. https://doi.org/10.1109/tns.2005.860748

Kim, M.-H. Y., Cucinotta, F. A., Nounu, H. N., Zeitlin, C., Hassler, D. M., Rafkin, S. C. R., et al. (2014). The MSL Science TeamComparison of martian surface ionizing radiation measurements from MSL-RAD with Badhwar-O'Neill 2011/HZETRN model calculations. *Journal of Geophysical Research: Planets*, *119*(6), 1311–1321. https://doi.org/10.1002/2013JE004549

Kim, M.-H. Y., Thibeault, S. A., Simonsen, L. C., & Wilson, J. W. (1998). Comparison of Martian meteorites and Martian regolith as shield materials for galactic cosmic rays (*NASA Langley technical report*).

Léveillé, R. J., & Datta, S. (2010). Lava tubes and basaltic caves as astrobiological targets on Earth and Mars: A review. *Planetary and Space Science*, *58*(4), 592–598. https://doi.org/10.1016/j.pss.2009.06.004

Masarik, J., & Reedy, R. C. (1996). Gamma ray production and transport in mars. *Journal of Geophysical Research: Planets*, *101*(E8), 18891–18912. https://doi.org/10.1029/96je01563

Matthiä, D., & Berger, T. (2017). The radiation environment on the surface of Mars–numerical calculations of the galactic component with GEANT4/planetocosmics. *Life Sciences and Space Research*, *14*, 57–63. https://doi.org/10.1016/j.lssr.2017.03.005

Matthiä, D., Ehresmann, B., Lohf, H., Köhler, J., Zeitlin, C., Appel, J., et al. (2016). The martian surface radiation environment–a comparison of models and MSL/RAD measurements. *Journal of Space Weather and Space Climate*, *6*(27), 1–17. https://doi.org/10.1051/swsc/2016008

Matthiä, D., Hassler, D. M., de Wet, W., Ehresmann, B., Firan, A., Flores-McLaughlin, J., et al. (2017). The radiation environment on the surface of Mars - Summary of model calculations and comparison to RAD data. *Life Sciences and Space Research*, *14*, 18–28. https://doi.org/10.1016/j.lssr.2017.06.003

O'Neill, P., Golge, S., & Slaba, T. (2015). *Badhwar–O'Neill 2014 galactic cosmic ray flux model*. (Technical report no. NASA/TP-2015.218569). Retrieved from https://ntrs.nasa.gov/archive/nasa/casi.ntrs.nasa.gov/20150003026.pdf

Potgieter, M. S. (2013). Solar modulation of cosmic rays. *Living Reviews in Solar Physics*, *10*(1), 1–66. https://doi.org/10.12942/lrsp-2013-3

Rafkin, S. C., Zeitlin, C., Ehresmann, B., Hassler, D., Guo, J., Köhler, J., et al. (2014). Diurnal variations of energetic particle radiation at the surface of Mars as observed by the Mars Science Laboratory Radiation Assessment Detector. *Journal of Geophysical Research: Planets*, *119*, 1345–1358. https://doi.org/10.1002/2013je004525

Richardson, I. G. (2004). Energetic Particles and Corotating Interaction Regions in the Solar Wind. *Space Science Reviews*, *111*, 267–376. https://doi.org/10.1023/B:SPAC.0000032689.52830.3e

Röstel, L., Guo, J., Banjac, S., Wimmer-Schweingruber, R. F., & Heber, B. (2020). Subsurface radiation environment of Mars and its implication for shielding protection of future habitats. *Journal of Geophysical Research: Planets*, *125*(3), e2019JE006246. https://doi.org/10.1029/2019JE006246

Roussos, E., Dialynas, K., Krupp, N., Kollmann, P., Paranicas, C., Roelof, E. C., et al. (2020). Long- and short-term variability of galactic cosmic-ray radial intensity gradients between 1 and 9.5 au: Observations by cassini, BESS, BESS-polar, PAMELA, and AMS-02. *The Astrophysical Journal*, *904*(2), 165. https://doi.org/10.3847/1538-4357/abc346

Saganti, P. B., Cucinotta, F. A., Wilson, J. W., Simonsen, L. C., & Zeitlin, C. (2004). Radiation climate map for analyzing risks to astronauts on the Mars surface from galactic cosmic rays. *Space Science Reviews*, *110*(1–2), 143–156. https://doi.org/10.1023/b:spac.0000021010.20082.1a

Simpson, J. (1983). Elemental and isotopic composition of the galactic cosmic rays. *Annual Review of Nuclear and Particle Science*, *33*(1), 323–382. https://doi.org/10.1146/annurev.ns.33.120183.001543

Starr, S. O., & Muscatello, A. C. (2020). Mars in situ resource utilization: A review. *Planetary and Space Science*, *182*, 104824. https://doi.org/10.1016/j.pss.2019.104824

Walsh, L., Schneider, U., Fogtman, A., Kausch, C., McKenna-Lawlor, S., Narici, L., et al. (2019). Research plans in Europe for radiation health hazard assessment in exploratory space missions. *Life Sciences and Space Research*, *21*, 73–82. https://doi.org/10.1016/j.lssr.2019.04.002

Wimmer-Schweingruber, R. F., Köhler, J., Hassler, D. M., Guo, J., Appel, J.-K., Zeitlin, C., et al. (2015). On determining the zenith angle dependence of the martian radiation environment at gale crater altitudes. *Geophysical Research Letters*, *42*(24), 10557–10564. https://doi.org/10.1002/2015gl066664

Zeitlin, C., Hassler, D. M., Wimmer-Schweingruber, R. F., Ehresmann, B., Appel, J., Berger, T., et al. (2016). Calibration and characterization of the Radiation Assessment Detector (RAD) on Curiosity. *Space Science Reviews*, *201*(1–4), 201–233. https://doi.org/10.1007/s11214-016-0303-y